Exploring the Outer Limits of Numerical Relativity

Carlos O. Lousto and Yosef Zlochower

Center for Computational Relativity and Gravitation,
School of Mathematical Sciences, Rochester Institute of Technology,
85 Lomb Memorial Drive, Rochester, New York 14623
(Dated: May 22, 2013)

We perform several black-hole binary evolutions using fully nonlinear numerical relativity techniques at separations large enough that low-order post-Newtonian expansions are expected to be accurate. As a case study, we evolve an equal-mass nonspinning black-hole binary from a quasicircular orbit at an initial coordinate separation of $D = 100M$ for three different resolutions. We find that the orbital period of this binary (in the numerical coordinates) is $T = 6422M$. The orbital motion agrees with post-Newtonian predictions to within 1%. Interestingly, we find that the time derivative of the coordinate separation is dominated by a purely gauge effect leading to an apparent contraction and expansion of the orbit at twice the orbital frequency. Based on these results, we improved our evolution techniques and studied a set of black hole binaries in quasi-circular orbits starting at $D = 20M$, $D = 50M$, and $D = 100M$ for $\sim$ 5, 3, and 2 orbits, respectively. We find good agreement between the numerical results and post-Newtonian predictions for the orbital frequency and radial decay rate, radiated energy and angular momentum, and waveform amplitude and phases. The results are relevant for the future computation of long-term waveforms to assist in the detection and analysis of gravitational waves by the next generation of detectors as well as the long-term simulations of black-hole binaries required to accurately model astrophysically realistic circumbinary accretion disks.

PACS numbers: 04.25.Dm, 04.25.Nx, 04.30.Db, 04.70.Bw

I. INTRODUCTION AND MOTIVATIONS

Ever since the breakthroughs in Numerical Relativity (NR) of 2005 [1–3], fully-nonlinear numerical simulations of merging black-hole binary (BHB) spacetimes have advanced at a remarkable pace. From a simulation perspective, BHB systems are characterized by the mass ratio ($q = m_1/m_2$), the individual spins of each BH ($\vec{S}_1, \vec{S}_2$), the initial separation ($\vec{D}$), and the momenta of each BH ($\vec{P}_1, \vec{P}_2$) (or equivalently the orbital eccentricity at some given separation). While all BHBs are computationally demanding, some of the interesting corners of the above parameter space remain particularly challenging. Initial investigations explored the orbital dynamics of similar-mass BHBs with low (or zero) spin, the computation of the associated gravitational radiation, and the characterization of final remnant products of their mergers. These techniques were soon expanded to study mixed systems of black holes (BHs) and neutron stars [4–7], the merger of neutron-star binaries (forming BHs) [8–10], gravitational collapse [11], and multiple black hole evolutions [12].

Notable progress has recently been made in simulating binaries with mass ratios as small as $q = 1/100$ in [13, 14], highly spinning black holes (with intrinsic spins $S/m^2 \geq 0.97$) [15], and ultra-relativistic collisions of black holes (reaching a Lorentz factor of $\gamma = 2.9$) [16].

The close limit of black holes in numerical relativity has been studied in detail by the 'Lazarus' approach [17–23]. In this paper we perform a first study of BHBs at relatively "large" (from the relativistic point of view) initial separations. While we expect this problem to be well described by the post-Newtonian approximations to general relativity, it is important to assess how well the current numerical relativity techniques model this case, and to what extent they have to be adapted or corrected to reach a given accuracy.

One of the main applications of the computation of accurate gravitational waveforms from BHBs is to assist gravitational wave observatories in detecting and analyzing gravitational radiation from astrophysical systems; merging BHBs being a primary target [24, 25]. With the enhanced low-frequency sensitivity of Advanced LIGO compared to initial LIGO, much longer waveform templates are required as binaries will stay in the low-frequency part of the advanced LIGO sensitivity band for a much longer period. In addition, the more stringent accuracy criteria needed to match full numerical waveforms to post-Newtonian (or other analytical waveforms) [26–31] require up to a factor ten more waveform cycles than is the current norm. To explore the future possibility of generating such waveforms (and even longer) by purely full numerical techniques, we consider the case of a BHB at an initial separation of $D = 100M$.

An independent motivation to study large-separation binaries comes from magnetohydrodynamics (MHD) studies of circumbinary disks around merging BHBs, which require many hundreds of orbital cycles before the accreting matter settles into a quasi-stationary state [32]. BHB evolution can either provide a background spacetime to evolve the MHD system, or the MHD and NR fields can be integrated in a self-consistent evolution.

In Sec. II, we describe our numerical techniques to evolve black hole binaries using the *moving puncture* ap-

proach [2]. In Sec. III, we describe the results of evolving a BHB starting at a separation of $D = 100M$ using the standard techniques developed for much closer binaries ($D \sim 10M$). We study the convergence of the orbital tracks of the holes for three resolutions (refined by successive factors of 1.2). We show results of new BHB simulations of $D = 100M$, $D = 50M$, and $D = 20M$ BHBs using improved evolution techniques in Sec. IV. We also include in our analysis the proper separation between the two BHs, its decay, and the gravitational waveforms extraction at (at least) one wavelength from the sources. We compare all results with 3.5 post-Newtonian predictions. We conclude in Sec. V that current full numerical techniques are able to accurately simulate the large separation regime but that the much longer time scales involved in the problem means that increases in simulations speeds by one to two orders of magnitude will be needed to complete the evolutions to merger.

II. NUMERICAL SIMULATIONS

We perform two different types of simulations here, a family of lower-accuracy, but high-speed, simulations of a BHB with initial separation of $D = 100M$ at different resolutions, and a family of higher-accuracy simulations at a fixed resolution but with different initial separations. Note, here and below we use M to denote the unit of distance, mass, energy, etc., while we use m to denote the mass of an object. To avoid confusion between the mass of a BHB and the mass of its constituent BHs, we denote the masses of each BH in a binary with a subscript.

We use the TwoPunctures thorn [33] to generate initial puncture data [34] for the BHB simulations described below. These data are characterized by mass parameters m_p (which are not the horizon masses), as well as the momentum and spin, of each BH. We evolve these BHB data sets using the LazEv [35] implementation of the moving puncture approach [2, 3] with the conformal function $W = \sqrt{\chi} = \exp(-2\phi)$ suggested by Ref. [36]. For the runs presented here, we use centered, eighth-order finite differencing in space [12] and a fourth-order Runge Kutta time integrator. (Note that we do not upwind the advection terms.) Our code uses the Cactus/EinsteinToolkit [37–39] infrastructure. We use the Carpet [40] mesh refinement driver to provide a "moving boxes" style of mesh refinement. In this approach refined grids of fixed size are arranged about the coordinate centers of both holes. The Carpet code then moves these fine grids about the computational domain by following the trajectories of the two BHs.

To reduce the computational costs, we performed an initial set of simulations (denoted by *generation 0* below) that use several low-accuracy approximations. Among them are the techniques introduced in Ref. [41] where the number of buffer zones at AMR boundaries is reduced by lowering the order of finite differencing by successive orders near the AMR boundaries (here we use 6

buffer zones), the use of simple interpolations of spectral initial data rather than using the complete spectral expansion [33], and the copying the initial data to the two past time levels for use in prolongation at the initial timestep. All of these approximation proved to be useful for reducing the cost of numerical simulations, but each one also has the side-effect of introducing a (hopefully) small $\mathcal{O}(h)$ error.

For our higher-accuracy simulations (denoted by *generation 1* below), we use a full complement of 16 buffer zones at refinement boundaries, use the full TwoPunctures spectral expansion to generate initial data, and use the Carpet init_3_timelevels option to populate the $t < 0$ timelevels required for prolongation. We also used a strict 2:1 refinement in time, which is required for the init_3_timelevels option. In addition, we placed the outer boundaries at $\sim 3000M$, far enough to obtain waveforms.

To compare the run speeds with and without the lower-order approximations, we performed two small runs using the grid structure and CFL factors of the *generation 1* simulations, one with the full complement of 16 buffer zones, and the other with only 6 buffer zones. The latter was faster by 28% (136 M /day compared to 106 M /day) The tests were performed on 20 nodes consisting of dual 6-core 3.47 GHz Nehalem CPUs. Increasing the CFL factor increases the run speed correspondingly (hence these low-accuracy techniques are quite useful in situations where high-accuracy is not required).

We use a modified 1+log lapse and a modified Γ-driver shift condition [2, 42, 43], and an initial lapse $\alpha(t = 0) = 2/(1 + \psi_{BL}^4)$, where ψ_{BL} is the Brill-Lindquist conformal factor and is given by

$$\psi_{BL} = 1 + \sum_{i=1}^{n} m_i^p/(2|\vec{r} - \vec{r}_i|),$$

where $\vec{r}_i$ is the coordinate location of puncture i. The lapse and shift are evolved with

$$(\partial_t - \beta^i \partial_i)\alpha = -2\alpha K, \tag{1a}$$
$$\partial_t \beta^a = (3/4)\tilde{\Gamma}^a - \sigma\beta^a, \tag{1b}$$

where we use $\sigma = 2$ for the *generation 0* simulations presented below, while we use a spatially varying $\sigma = (\sigma_0 - \sigma_\infty)\exp(-r^4/w^4) + \sigma_\infty$ (where $\sigma_0 = 2.0$, $\sigma_\infty = 0.25$, $w = 80.0$) for the *generation 1* simulations. The reason for the differences is that, since we use strict 2:1 refinement in time for *generation 1*, we need a small σ at large distances in order for the system to remain stable [44].

We use AHFinderDirect [45] to locate apparent horizons. Here the spins of the two BHs are negligible and the horizon mass is equal to the irreducible mass (i.e. $m_{\rm irr} = \sqrt{A/(16\pi)}$, where A is the surface area of the horizon).

III. ZEROTH GENERATION RUNS

Here we use our standard full numerical techniques (developed to evolve BHB at initial separations $D \sim 10M$) to evolve a BHB at a separation of $D = 100M$ and compare with the post-Newtonian predictions for the orbital trajectory.

A. Quasicircular Post-Newtonian Analysis

BHB quasicircular orbits at separations $r \sim 100M$ (note that we use r to denote the post-Newtonian (PN) expression for the orbital separation) should be described accurately by the 2PN [46] expressions for the orbital frequency

$$\Omega^2 = \frac{m}{r^3}\left[1 - (3 - \eta)\frac{m}{r} + \left(6 + \frac{41}{4}\eta + \eta^2\right)\frac{m^2}{r^2}\right] + \cdots \tag{2}$$

and radial decay of the orbit (due to energy loss)

$$\dot{r} = -\frac{64M^3}{5r^3}\eta\left[1 - \frac{(1751 + 588\eta)}{336}\frac{m}{r} + 4\pi\left(\frac{m}{r}\right)^{3/2}\right] + \cdots, \tag{3}$$

where $m = m_1 + m_2$ is the total mass and $\eta = (m_1 m_2)/m^2$. The orbital period, T, at $r = 100M$ for an equal-mass BHB is given by

$$T = \frac{2\pi}{\Omega} \approx 6369M, \tag{4}$$

where $m\Omega \approx 0.001$, and $m = 1M$.

We thus estimate that the radial decay after one orbit is

$$\Delta r = \dot{r}T \approx -0.02M. \tag{5}$$

Note that in the above expressions r is the harmonic radial coordinate, which is related to the ADM-TT coordinate R (initially related to the numerical coordinates) by [66] $r = R + m^2(2 + 29\eta)/(8R) + \cdots$. We also neglect the effects of the small eccentricities that are present in the full numerical runs.

B. $D = 100M$ Runs versus resolution

In order to generate initial data, we need the puncture (coordinate) separation and momenta. We obtain approximations for the separation and momenta by using the associated 3.5PN parameters. Our procedure is as follows: We start with 3.0 PN quasi-circular parameters for an orbital separation of $D \sim 100M$. We then perform a 3.5PN evolution [47–49] of the orbital motion. The resulting orbit will be (moderately) eccentric. We then use the procedure in [50] to obtain successively better approximations of the initial momenta for this 3.5PN evolution until the eccentricity is reduced to the roundoff

TABLE I: Initial data parameters for the full numerical simulations. The punctures are located at $\pm(x, 0, 0)$, with momenta $\pm(p_x, p_y, 0)$, spin $(0, 0, 0)$, and puncture mass m_p. m_H is the measured horizon masses, while T_i is the period of the first orbit for the three resolution runs (0 for coarsest, 1 for medium, 2 for finest). $m_{\rm PN}$ and $T_{\rm PN}$ are the corresponding post-Newtonian values

$x = 50$	$T_{\rm PN} = 6365$
$p_x = -7.97939 \times 10^{-7}$	$T_0 = 6406$
$p_y = 2.55526 \times 10^{-2}$	$T_1 = 6420$
$m_p = 0.49920645$	$T_2 = 6422$
$m_H = 0.500615$	$m_{\rm PN} = 0.500616$

TABLE II: The grid structure for the three numerical simulations presented here. The coarsest run had $h = h_0 = 4M$, while the two higher resolution runs had $h = h_1 = 4M/1.2$ and $h = h_2 = 4M/1.44$, respectively.

	radius	resolution	CFL
0	400	h	0.019
1	220	$h/2$	0.038
2	110	$h/4$	0.076
3	55	$h/8$	0.152
4	25	$h/16$	0.152
5	10	$h/32$	0.304
6	5	$h/64$	0.304
7	2	$h/128$	0.304
8	0.65	$h/256$	0.304

limit. After renormalizing to an ADM mass of $1M$, we use the resulting PN parameters to solve for the initial data. The parameters are given in Table I.

We evolved the binary at three different resolutions characterized by a coarse-level resolution of $h_0 = 4M$, $h_1 = 4M/1.2$, and $h_2 = M/1.44$, respectively. For these runs, we choose a Courant-Friedrichs-Lewy (CFL) factor (i.e. the ratio dt/h between the timestep and gridsize) that varies with refinement level, as described in Table II. In all cases, the boundaries were located at $400M$ and 9 levels of (2:1) refinement were used. This means that the boundary is causally connected to the binary for most of the simulation.

As seen in Fig. 1, the trajectory of the full numerical simulation is almost a closed circle with radius $r \sim 100M$. A more quantitative comparison is shown in Fig 2, where we plot the orbital frequency as a function of orbital separation and compare to the 3.5PN predictions. As seen in Fig 2, the orbital frequency starts out much lower than predicted (which is purely a gauge effect) and then approaches the PN value from below.

A closer look at the time dependence of the coordinate separation (and its time derivative) shows the limited accuracy of the runs. A pure 3.5PN evolution indicates that this binary will take approximately $t \sim 8.2 \times 10^6 M$ to inspiral to an orbital separation of $r = 5M$. During the first orbit, the 3.5PN binary inspirals only $0.02M$ from the initial separation of $r = 100M$. As shown below, the full
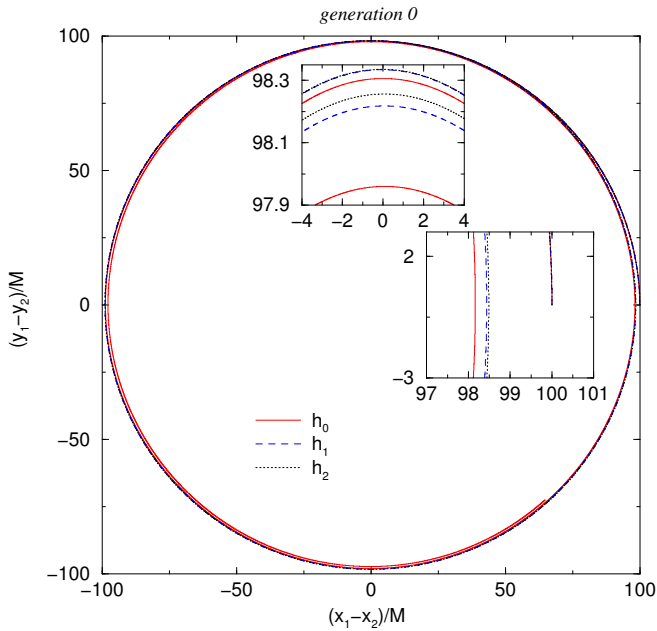
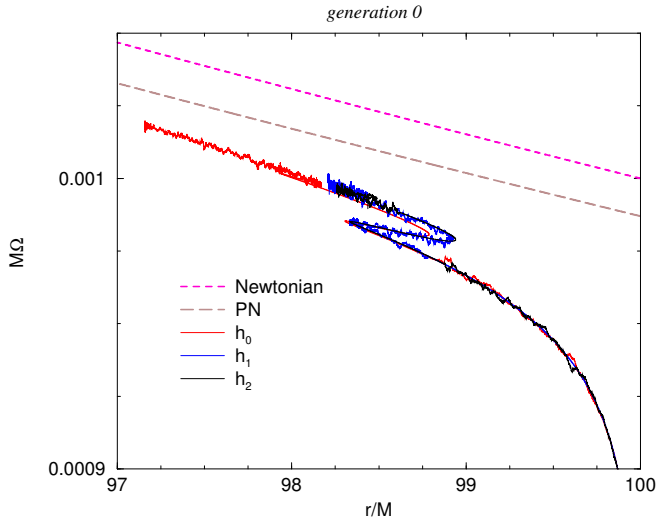FIG. 1: The orbital trajectory for the *generation 0 D = 100M* simulations at different resolutions.

FIG. 2: The orbital frequency $d\phi_{\rm orbit}/dt$ versus orbital separation r, as well as the Newtonian and 3.5 PN predictions for the *generation 0 D = 100M* simulations. The mapping between r and Ω is not unique because r is not a monotonic function of t.

FIG. 3: The orbital separation versus time at three resolutions, as well as the 3.5PN prediction, for the *generation 0 D = 100M* simulations.

FIG. 4: The orbital frequency versus time at three resolutions, as well as the 3.5PN prediction, for the *generation 0 D = 100M* simulations..

numerical binaries inspiral by two orders of magnitude more. While the 3.5PN simulation indicates that this binary is not eccentric, there are significant oscillations in the orbital radius (usually associated with eccentricity). Interestingly, these oscillations occur at twice the orbital frequency (see Fig. 3), while for eccentricity effects we expect oscillations at the orbital frequency. In Figs. 3 and 4, we plot the orbital separation and frequency versus time and compare to the PN prediction. Again, a significant
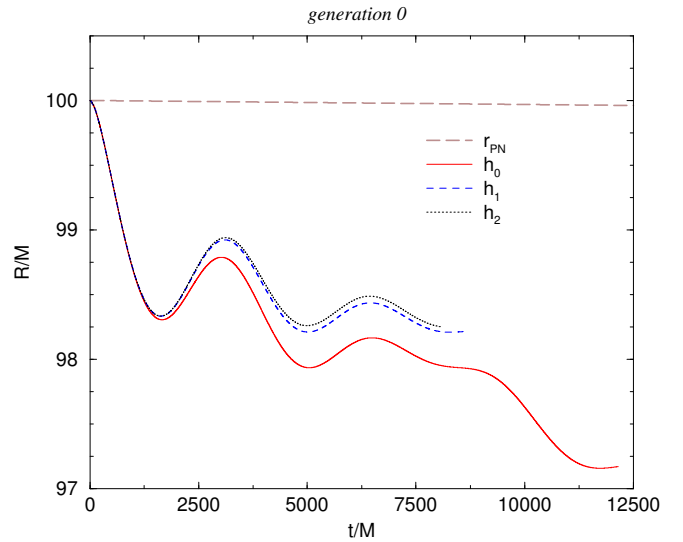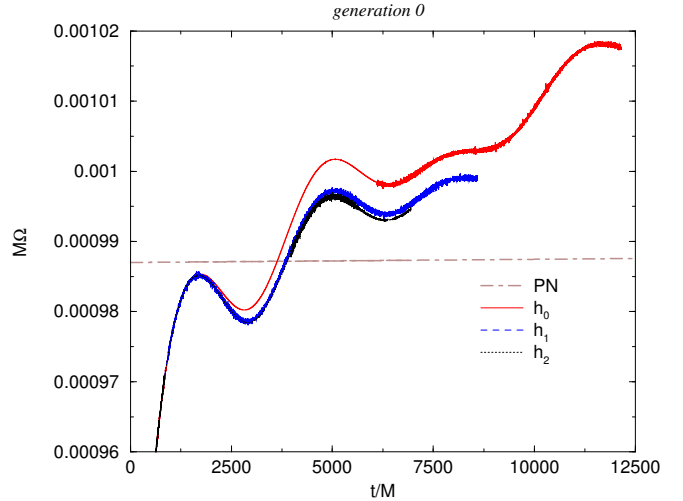
difference between the PN and numerical results is apparent. We will show in the next section that this behavior is mostly a coordinate artifact and proper distance measurements greatly ameliorate this issue. The coordinate artifact may be produced by the zero speed gauge mode [43] contained in our choice of the shift condition (1b).

In a previous study [51], we found that unphysical increases or decreases in the horizon mass can have a significant impact on the orbital trajectory. In Fig. 5 we plot the horizon mass as a function of resolution versus time. We observe an increase in mass, which may be the cause of the artificial inspiral. The mass increase is small, but this secular growth (which gets worse as the resolution
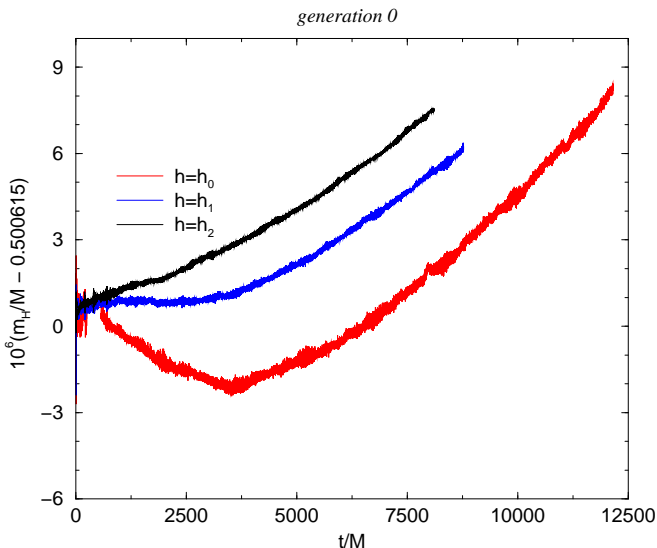
FIG. 5: The horizon mass of the individual BHs versus time of the *generation 0* simulations for the three resolutions. Both the secular growth with time for all resolution, and the growth in mass as the gridspacing is reduced, indicate a loss of accuracy at later times for these *generation 0* simulations.
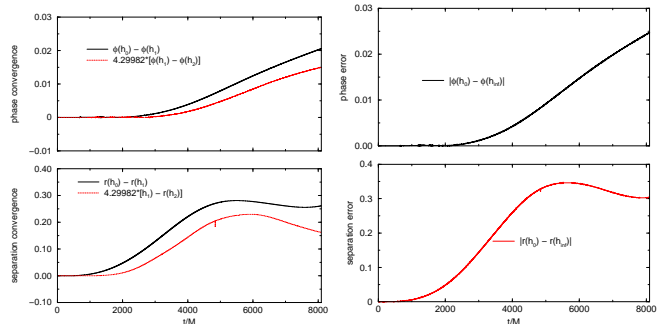

FIG. 6: (Left) Convergence plots for the orbital phase (top-left) and separation (bottom-left) showing stronger than eighth-order convergence. If a quantity $F(h)$ is eighth-order convergent, then $F(h_0) - F(h_1) = 4.29982[F(h_1) - F(h_2)]$. Here we see *hyperconvergence*, which almost certainly means that the errors is oscillating with h rather than behaving monotonically. The top-right plot shows the phase error of the coarsest resolution run (assuming eighth-order convergence and comparing the Richardson extrapolated value), while the bottom-right plot shows the orbital separation error.

is increased) can affect the accuracy of longer term runs. We will see how to better control this artifact in the next section.

Finally, as seen in Fig. 6, the convergence order, as measured by comparing the differences in the orbital separations and phase between the h_0 and h_1 runs and the h_1 and h_2 runs, appears to be higher than eighth order. In the past, when we encountered this apparent super convergence, we found in the end that the error was an oscillatory function of the grid resolution (see [52]). However, if we attempt to extrapolate, assuming eighth-order convergence, we find that the error in the orbital separation increases to about $0.34M$ and then appears to level off. The phase error increases to about 0.025 rad.

IV. FIRST GENERATION RUNS

In our study of waveform accuracy for closer BHBs [52], we found that the low-accuracy approximations used in our *generation 0* simulations may have a larger impact than expected. As seen in Fig. 5, mass gain is an issue for *generation 0*. By *correctly* initializing the grid and by lowering the CFL factor to 0.25, we mitigate this mass loss issue. Importantly, we also place the outer boundaries a factor of ~ 10 farther away. Note that it is the CFL factor in the inner regions (near each BH) that is responsible for the conservation (or lack thereof) of the BH mass. So even though the *generation 1* runs have a larger CFL factor in the outer zones then the *generation 0* runs, they are still more accurate in terms of mass preservation.

As an additional analysis tool, we use the proper distance between the two horizons as measured along the coordinate line joining the two punctures [53], which we call the *semiproper distance*, or SPD, below (note that the minimal geodesic does not follow this line).

For the *generation 1* runs, we performed simulations with a grid structure similar to the low resolution h_0 *generation 0* run, but with several additional coarser levels, and studied BHBs with initial orbital separations of $D = 20M$, $D = 50M$, and $D = 100M$. We placed the outer boundaries at $3200M$ and used 14 levels of refinement with a coarsest resolution of $h = 32M$ (extending the grid to $6400M$ stably can be achieved by halving the gauge baseline σ_∞ or extending the grid without refining it by a factor 2 or halving the CFL condition). We used strict 2:1 refinement in time and a full complement of 16 buffer zones at the boundary of each refinement level.

The conservation of the BH masses during the evolution is an important indicator of the accuracy of the full numerical runs, and is particularly important for long term evolutions. We show the horizon mass for the $D = 100M$ *generation 1* run and compare with the *generation 0* runs in Fig. 7. We observe that while *generation 0* runs show an strong growth of the masses with time and with increasing resolution, the profile of the *generation 1* runs is rather flat, and we expect this to be still the case for higher resolutions as observed in Ref. [52], Fig. 2.

A. Varying the BHB initial separation

On of the robust features of both our *generation 0* and *generation 1* runs is the approach of the full numerical orbital frequency to the PN predicted values from be-
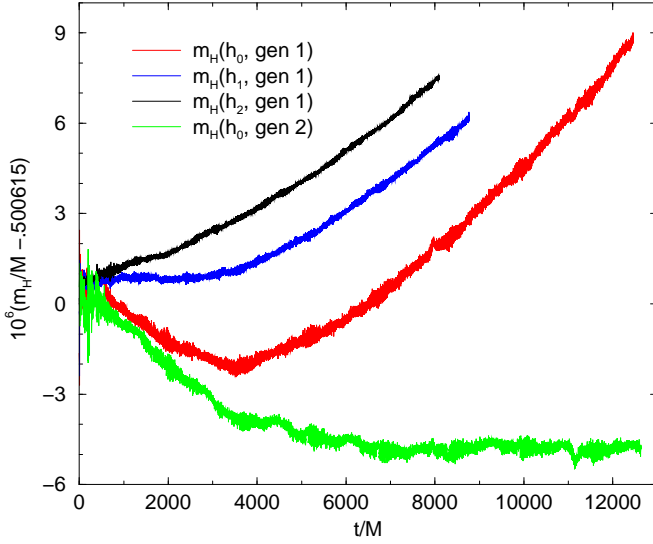
FIG. 7: Comparing the $D = 100M$ mass conservation for the *generation 0* and *generation 1* runs. Note that the *generation 1* simulation shows no late time growth. The conservation of the mass at levels of below 1 part in 10^5 is crucial for long term evolutions.

TABLE III: The eccentricity and orbital period of the numerical simulations, the 3 PN quasicircular orbital periods at the initial separation and separation after one orbit, and the 3.5 PN orbital inspiral after one orbit.

D/M	e_s	T_{NR}/M	T_{PN}/M	$\Delta r/M$
20	0.0003	615	601-592	-0.208
50	0.0002	2313	2283-2279	-0.054
100	0.0006	6422	6370-6368	-0.02

low (after the numerical coordinate *settle* into a quasistationary regime [which takes ~ 1 orbit]). For the $D = 20M$ case (see Fig. 8), the numerical and PN predictions agree to two significant digits (e.g., $\Omega_{\mathrm{PN}} = 0.01142$, while $\Omega_{\mathrm{num}} = 0.01125$, at $D = 18.84M$) after the gauge settles down. The progression is similar for the cases of orbits starting at separations $D = 50M$ and $D = 100M$, where the simulations completed 2.5 and 1.5 orbits, respectively. The retrograde features in these figures are due to the remaining (small) eccentricity of the initial quasicircular data and gauge effects. We report in Table III the eccentricities of these BHBs, as measured via the formula $e_s \sim s^2\ddot{s}$, where $s(t)$ is the *semiproper distance*, as well as the measured orbital period and the 3 PN prediction, including the decay rate Δr after one orbital period.

As we saw in the *generation 0* runs (see Fig. 3), the coordinate separation of the holes shows an interesting gauge effect, namely an oscillation in time at twice the expected frequency. In order to show that this is a nonphysical effect, we computed the proper distance along the line joining the black holes, i.e., the SPD measure described above (we use this measure since an accurate
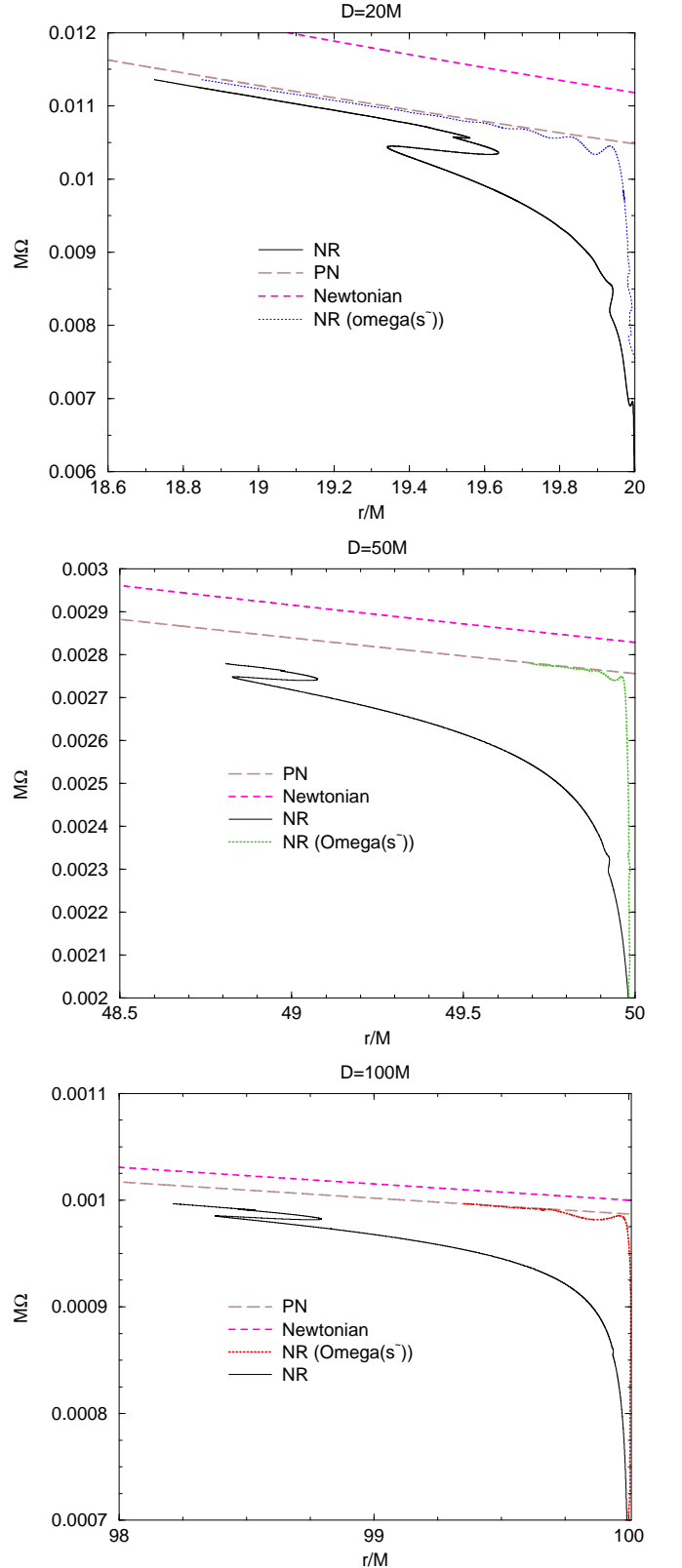

FIG. 8: The orbital frequency $d\phi_{\mathrm{orbit}}/dt$ versus orbital separation r and versus *shifted semiproper distance* $\tilde{s}$, as well as the Newtonian and 3.5 PN predictions for the $D = 20M, 50M, 100M$ *generation 1* runs. Here $\tilde{s} = s - (s_0 - r_0)$, where s_0 is the initial SPD and r_0 is the initial PN orbital separation.

minimal proper distance between horizons is computationally very intensive). The results are shown in Fig. 9. We first observe that the proper distance is much closer to being monotonic and featureless than the coordinate separation. We also see that there are residual oscillations (of much lower amplitude than those observed in the coordinate separation) at roughly the orbital frequency, which likely are due to the eccentricity, as well as a possible small residual gauge effect.

In Fig. 9, we subtract a constant offset from the proper distances in order to make comparison with the coordinate separation easier. We see the striking agreement (apart from the overall constant offset between the two) at later times, i.e. after the first orbit, showing that the coordinate gauge effects settle down after one cycle, quite independent from the initial radius of the orbit, i.e. in all cases studied, $D/M = 20, 50, 100$.

In Fig. 10, we compare the orbital frequency, as a function of time, for the *generation 0* and *generation 1* ($D = 100M$) simulations. Note how the *generation 1* appears to outperform the highest resolution *generation 0* run.

Using our more accurate *generation 1* simulations, and the SPD measure of the orbital separation, we study in more detail the orbital decay of the numerical runs and compare them with the PN predictions. Here were examine $\dot{s}(t)$ as a function of time, where $s(t)$ is the SPD. In Fig. 11 we see the good agreement between the mean values of $\dot{s}(t)$ and the 3.5PN predictions. The agreement is slightly better for the closer $D/M = 20$ case, which we evolved for three orbits, than for the more demanding $D/M = 50, 100$ cases, which did not complete two orbits. There is an oscillation corresponding closely to the orbital period of the $D/M = 20, 50, 100$ runs (according to PN, $T/M = 598, 2281, 6369$, respectively). Note that in Fig. 11 we used the same ordinate scale and therefore the amplitudes of oscillations are comparable, which indicates that the eccentricities of the farther separated BHBs are larger.

In order to have a visual notion of how tight the orbits look in proper distance s space, we plot the *semiproper* trajectory $\vec{r}(\phi) = s(\cos\phi, \sin\phi)$. Here ϕ is the coordinate azimuthal angle, while s is the SPD. Our results are shown in Fig. 12. The scale of the zoom-in plots is the same for all runs (making comparison of the relative tightness of the orbits straightforward). Note that the larger separation between successive orbits for the $D = 100M$ case than for the $D = 50M$ case likely reflects some combination of residual gauge effects and truncation errors (see Fig. 11). While the $D = 100M$ orbital decay rate appears to be too large by a factor of 2-3, the gauge invariant radiated energy is consistent with PN predictions (see Sec. IV B and Fig. 11).

We note that, according to 3.5PN evolutions, the $D = 20M$ BHB completes 36 orbits and takes $t = 14,200M$ to inspiral to $D = 5M$. The $D = 50M$ BHB, on the other hand completes 370 orbits and takes $t = 531,716M$ to get to the same separation. Finally, the $D = 100M$ BHB
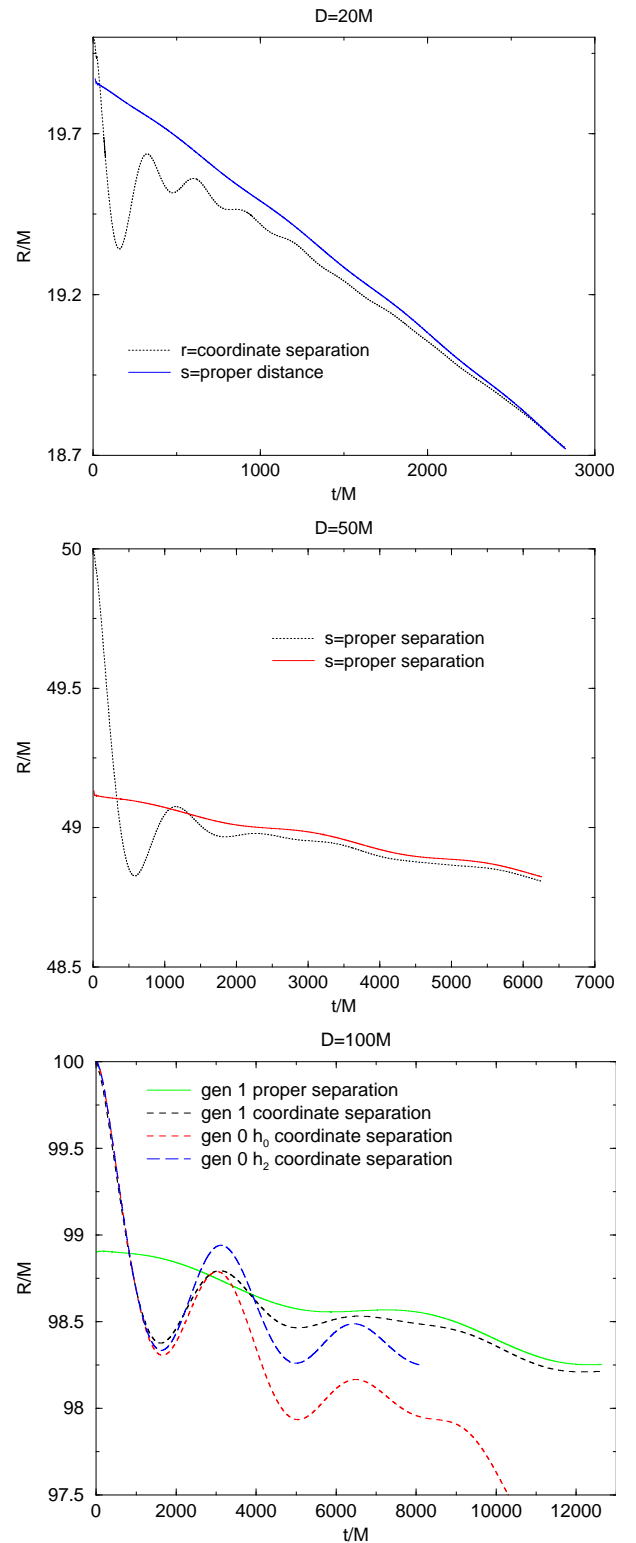

FIG. 9: Proper distance (minus a constant) and coordinate distance comparison for the $D = 20M, 50M, 100M$ *generation 1* runs. The $D = 100M$ plot also shows the coordinate separation versus time for the *generation 0* runs.
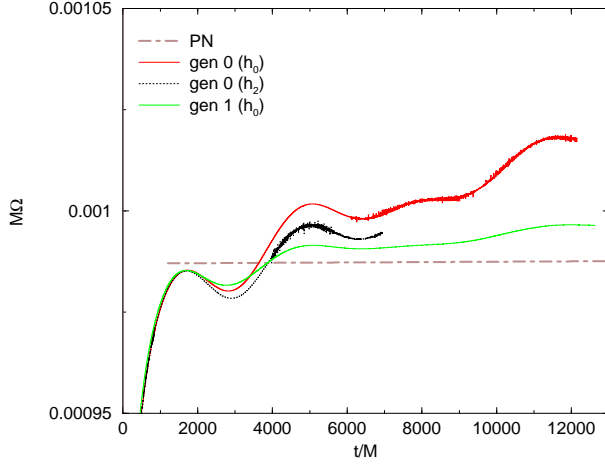
FIG. 10: The orbital frequency for the *generation 0* and *generation 1* runs versus time ($D = 100M$) and the PN prediction. Note how the *generation 1* appears to outperform the highest resolution *generation 0* run.

completes 2064 orbits and takes $t = 8,223,170M$.

B. Comparison with Post-Newtonian waveforms

The leading $(2,2)$-mode of the PN waveform [54] is given by

$$r_{\rm obs}\, h^{(2,2)} = -8m\sqrt{\frac{\pi}{5}}\,\eta\, x\, H^{(2,2)} e^{-2i\psi} \qquad (6)$$

where $\psi = \varphi - 2M\Omega \ln(\Omega/\Omega_0)$, φ is the orbital phase,

$$
\begin{aligned}
H^{(2,2)} &= 1 + \left(-\frac{107}{42} + \frac{55}{42}\eta\right) x + 2\pi\, x^{3/2} \\
&+ \left(-\frac{2173}{1512} - \frac{1069}{216}\eta + \frac{2047}{1512}\eta^2\right) x^2 \qquad (7)\\
&+ \left(-\frac{107}{21}\pi + \frac{34}{21}\pi\eta - 24i\eta\right) x^{5/2} + \cdots
\end{aligned}
$$

$x = (m\Omega)^{2/3}$, and Ω_0 is an arbitrary positive constant (see [54]) which we took to be the initial orbital frequency. For quasicircular orbits, up to 3 PN, the orbital frequency is given by [67]

$$
\begin{aligned}
m\Omega &= \left(\frac{m}{R}\right)^{3/2}\Bigg[1 + \frac{(\eta - 3)}{2}\left(\frac{m}{R}\right) \\
&+ \frac{(6\eta^2 + 7\eta + 24)}{16}\left(\frac{m}{R}\right)^2 \\
&+ \frac{(120\eta^3 - 612\eta^2 + 501\pi^2\eta - 8096\eta - 480)}{384}\left(\frac{m}{R}\right)^3 \\
&+ \cdots\Bigg],
\end{aligned} \qquad (8)
$$

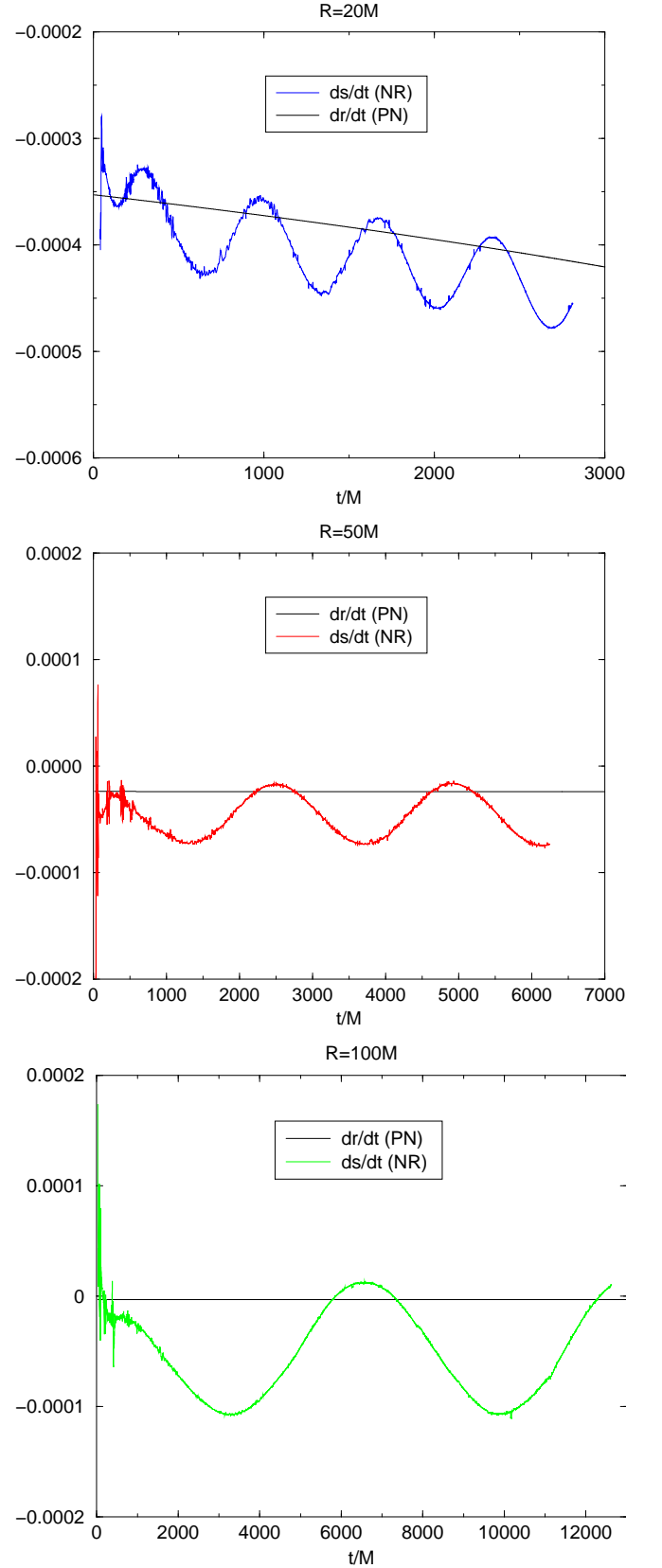where R denotes the ADM-TT radial coordinate.

FIG. 11: Simple proper distance decay rate versus post-Newtonian prediction for the $D = 20M$, $D = 50M$, and $D = 100M$ *generation 1* runs. Note that the periods of oscillations roughly match those of the orbital period, $T/M = 598, 2281, 6369$ respectively
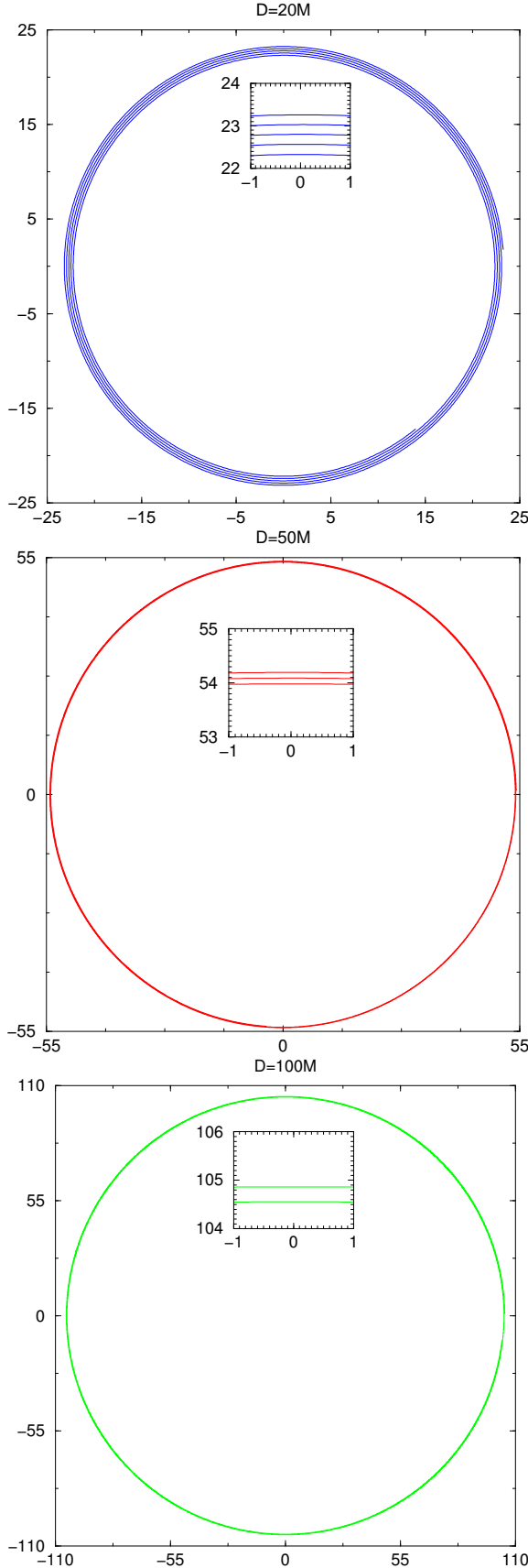
FIG. 12: The orbital *trajectory* obtained using the coordinate orbital phase and the *proper* orbital separation along the coordinate line separating the two BHs for the *generation 1* simulations. The zoomed plots show the tightness of the spiral.

For large r, ψ_4 is given by [55]

$$\psi_4 = \frac{1}{2}\left(\ddot{h}_+ - i\ddot{h}_\times\right) \approx -2m^2\Omega^2 h^{(2,2)}. \qquad (9)$$

The radiated energy and angular momentum are give by Eqs. (7.4a)-(7.4b) of Ref. [56]

$$\frac{dE}{dt} = \frac{32}{5}\eta^2 x^5 \left\{1 - \left(\frac{1247}{336} + \frac{35}{12}\eta\right)x + 4\pi x^{3/2}\right.$$
$$+\left(-\frac{44711}{9072} + \frac{9271}{504}\eta + \frac{65}{18}\eta^2\right)x^2$$
$$\left.+\left(-\frac{8191}{672} - \frac{583}{24}\eta\right)x^{5/2}\right\} + \cdots \qquad (10a)$$

$$\frac{dJ}{dt} = \frac{32}{5}m\eta^2 x^{7/2} \left\{1 - \left(\frac{1247}{336} + \frac{35}{12}\eta\right)x\right.$$
$$+4\pi x^{3/2} + \left(-\frac{44711}{9072} + \frac{9271}{504}\eta + \frac{65}{18}\eta^2\right)x^2$$
$$\left.+\left(-\frac{8191}{672} - \frac{583}{24}\eta\right)x^{5/2}\right\} + \cdots \qquad (10b)$$

where $\frac{dE}{dt} = \Omega\frac{dJ}{dt}$ for quasicircular orbits. Hence, we can approximate the energy E and angular momentum J radiated per quasicircular orbit by

$$\delta E = \int_0^T \frac{dE}{dt}dt \approx \frac{dE}{dt}T = \frac{dE}{dt}\frac{2\pi}{\Omega}, \qquad (11)$$

with a similar expression for the radiated angular momentum (where the integral is over the time interval corresponding to two complete cycles of the ($\ell = 2, m = 2$) mode of ψ_4, and hence one orbit of the BHB).

Comparisons between full numerical and PN waveforms can provide a strong test of both approaches. For the *generation 1* runs, we extended the computational domain to a cube of sides $6400M$ in order to be able to extract the gravitational waveforms in the *radiation zone*. The effects of the extraction radii on the amplitude and phase of the numerical waveforms is apparent in Fig. 13, where we plot the $D = 20M$ the waveforms as seen by observers at $R_{\text{obs}}/M = 100, 300, 400, 800$. Note that in this case, the half orbital period (measuring the period of the waves) is $\approx 300M$. We see that extracting at $R_{\text{obs}}/M = 100$ leads to inaccuracies in both the amplitude and phase, but for $R_{\text{obs}}/M = 300, 400, 800$ the waveforms line up; indicating that extracting at least at one wavelength from the system is necessary. In all cases, we used the perturbative extrapolation formula given in Ref. [57].

$$\lim_{r\to\infty}\left[r\,\psi_4^{\ell m}(r,t)\right]$$
$$= \left[r\,\psi_4^{\ell m}(r,t) - \frac{(\ell-1)(\ell+2)}{2}\int_0^t dt\,\psi_4^{\ell m}(r,t)\right]_{r=R_{\text{obs}}}$$
$$+O(R_{\text{obs}}^{-2}), \qquad (12)$$

where for our choice to the tetrad we have $\psi_4 = (1/2 - M/r)\psi_4^{\text{Num}}$. For larger orbital separations the orbital pe-
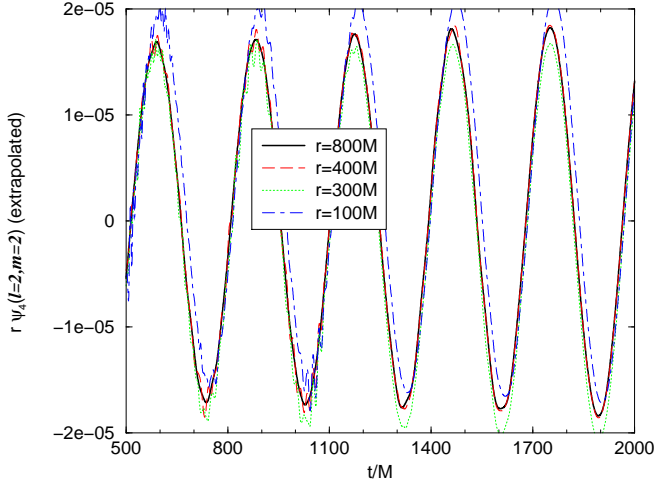
FIG. 13: The waveform extracted at different observer locations for the $D = 20M$ *generation 1* run. Here the waveforms have been *extrapolated to* ∞ using Eq. (12). While we see that the extraction at $R_{\mathrm{obs}} = 100$ has large phase errors, the phases and amplitudes stabilize for $R_{\mathrm{obs}} \geq 300$, i.e. one wavelength distance from the sources.
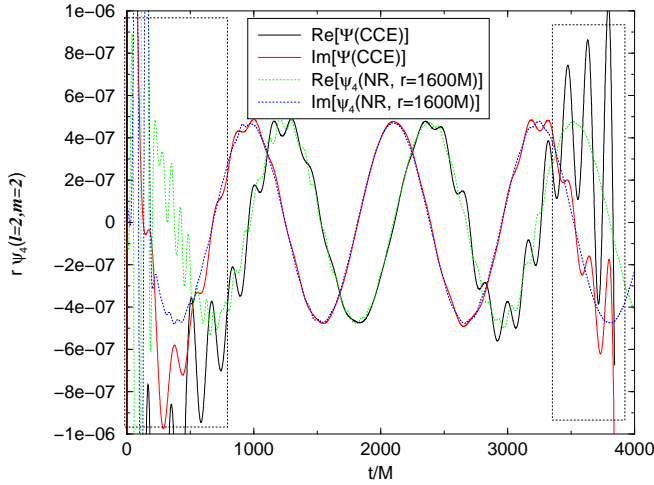

FIG. 14: Comparison of $r\psi_4$ and the Null variable Ψ for the $D = 50M$ simulation. The boxes indicate regions where the fast Fourier transform smoothing operation on the CCE data distorted the waveform.

riod increases (See Eqs. (2-4)) approximately as $\sim D^{3/2}$ hence we need observer locations of at least $R_{\mathrm{obs}}/M = 1150$ and $R_{\mathrm{obs}}/M = 3200$, respectively, for binaries with separations $D/M = 50$ and $D/M = 100$. In Fig. 14, as an independent validation of the finite radius extraction, we compare the perturbative extraction as defined above (12) with the Cauchy characteristic extraction (CCE) code described in Ref. [58] and observe the good agreement among them in the common region of validity.

We find a striking agreement (particularly at larger separations) between these full numerical waveforms and the PN waveforms given by Eq. (9). In Fig. 15 we plot

TABLE IV: Energy and angular momentum radiated per orbit (initial and second).

D	$\delta m / M_{\mathrm{num}}$	$\delta m / M_{\mathrm{PN}}$
20M	$(5.68 \pm 0.02) \times 10^{-5}$	$5.43 - 5.62 \times 10^{-5}$
50M	$(2.4 \pm 0.1) \times 10^{-6}$	$2.52 - 2.53 \times 10^{-6}$
100M	$(2.3 \pm 0.4) \times 10^{-7}$	$2.36 - 2.36 \times 10^{-7}$
D	$\delta J / M_{\mathrm{num}}^2$	$\delta J / M_{\mathrm{PN}}^2$
20M	$(5.39 \pm 0.01) \times 10^{-3}$	$5.20 - 5.30 \times 10^{-3}$
50M	$(8.9 \pm 0.1) \times 10^{-4}$	$9.16 - 9.18 \times 10^{-4}$
100M	$(2.4 \pm 0.4) \times 10^{-4}$	$2.39 - 2.39 \times 10^{-4}$

$R\psi_4$ extrapolated using Eq. (12) and the 3.5PN [55] prediction. The differences in the phase and amplitudes are within the numerical noise. For the $D = 20$ case, we still observe improvements between the 2PN expression, as truncated in Eq. (7), and the 3.5PN expression. At the larger initial separations, $D = 50M, 100M$, even the lower-order PN expressions [i.e. Eq. (7)] show excellent agreement with the full numerical waveform.

We note that based on the *generation 0* convergence simulations, we may expect that the orbital phase error in the $D = 100M$ simulation run is under 0.025 rad (the argument being that the *generation 1* simulations should be more accurate at a given resolution than the *generation 0* simulations). Based on the observed agreement between the PN and NR simulation, it appears that the phase error is indeed (relatively) small.

Finally, we give the energy and angular momentum radiated, per orbit, in Table IV. For the table, we measure the energy and angular momentum radiated over one period of the $(\ell = 2, m = 2)$ mode (however, we use all modes up to $\ell = 4$ to calculate the energy and angular momentum radiated), we then multiply by 2 (we do this because we do not have two full cycles at $R_{\mathrm{obs}} = 3000M$ for $D = 100M$). We approximate the error in these measurements by calculating δm and δJ at $R_{\mathrm{obs}} = 3000M$ ($R_{\mathrm{obs}} = 1600M$ for $D = 20M$) and $R_{\mathrm{obs}} = 1500M$ ($R_{\mathrm{obs}} = 800M$ for $D = 20M$) and take the difference between these two measurements as the error. We compute the energy and angular momentum radiated at the initial separation and after one orbit including the radial decay given by $\Delta r \approx \langle \frac{\mathrm{d}a_r}{\mathrm{d}t} \rangle T$, where [56]

$$
\left\langle \frac{\mathrm{d}a_r}{\mathrm{d}t} \right\rangle = -\frac{64}{5} c x^3 \eta \left\{ 1 + \left(-\frac{743}{336} - \frac{11}{4}\eta \right) x + 4\pi \, x^{3/2} \right.
$$
$$
+ \left(\frac{38\,639}{18\,144} + \frac{11\,393}{2016}\eta + \frac{19}{6}\eta^2 \right) x^2
$$
$$
\left. + \pi \left(-\frac{4159}{672} - \frac{189}{8}\eta \right) x^{5/2} + \cdots \right\}. \quad (13)
$$

V. DISCUSSION

We performed a first exploration of full numerical evolutions of a black-hole binaries with large initial sepa-
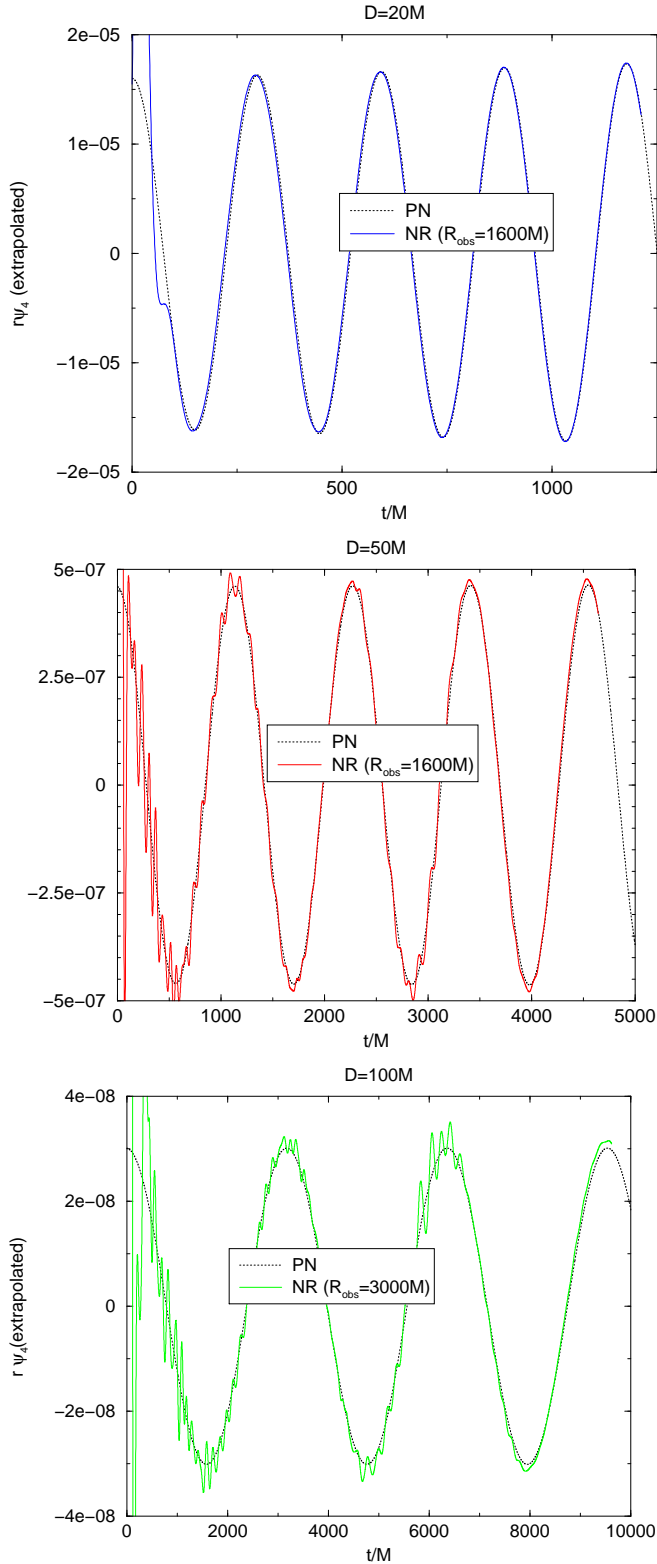
FIG. 15: Comparison of 3.5PN and full numerical waveforms for the $D = 20M, 50M, 100M$ *generation 1* simulations. Note the excellent agreement in both amplitude and phase and the very small scale of the amplitudes.

rations in order to evaluate how numerical techniques developed for close binaries (initial separations of around $R \sim 10M$) handle this regime. We studied a prototypical binary with an initial separation of $D = 100M$. Given the large orbital period involved ($T \approx 6400M$), we restricted our evolutions to the first few orbits. We find that the full numerical simulations agree with the post-Newtonian predictions for the gravitational waveform, orbital frequencies, orbital decay rate, and radiated energy. These are nontrivial features given the length scales involved in the problem and the very small amplitude of the radiation.

From these first studies we can draw several conclusions:

i) The initial pulse of spurious radiation (and gauge relaxation) still requires a period of the order of one orbital cycle to settle (that seems to be quite independent of the initial orbital radii). This implies longer evolution times to obtain accurate waveform information. Alternatively, one could use initial data with some information of the realistic radiation content along the lines of Ref. [59].

ii) Given the long evolution times required and the long wavelengths involved, the location of the computational boundaries should allow for the extraction of radiation at (at least) one wavelength from the sources. We note that more efficient techniques to treat the evolution in this *far* zone include the use of more accurate boundary conditions [60], multi-patch schemes [61], and the choice of coordinates that are better adapted to the problem [17].

iii) A pure 3.5PN evolution indicates that this binary will take approximately $t \sim 8.2 \times 10^6 M$ to inspiral to an orbital separation of $D = 5M$. During this inspiral, the binary would complete 2064 orbits. Our full numerical simulations on 20 nodes (3.46GHz dual Intel processors with 6 cores each) produced an average evolution of nearly $100M$ per day. This would led to a total of over 200 years to complete the evolution. Dramatic improvements in the speed of the evolution codes, possibly using use hardware accelerators [62], or novel numerical techniques, such as implicit-explicit methods [63], will be needed in order to make simulations from these separations to mergers possible.

iv) Based on the *generation 1* results and our results in [52], we can foresee a *generation 2* set of runs that use the current runs to reduce eccentricity using for instance the method [50], have the computational boundaries moved to even larger radii (which would require setting σ_∞ to a smaller value), use higher-order AMR prolongation and numerical dissipation, and replace the *semiproper distance* with the proper distance of the shortest geodesic joining the two horizons.

We note that the eccentricity reduction method of [50], when applied to $\dot{s}(t)$ for the $D = 100M$ configuration, gives a very small change in the initial tangential momentum and a very large change in the initial radial momentum. In particular, we find $\delta p_t/p_t = 6.056 \times 10^{-6}$ and $\delta p_r/p_r = 18.6$. The latter result is surprising as

it is not consistent with the magnitude of the PN radial momentum. We speculate that this indicates that the oscillations in $\dot{s}(t)$ are not due to purely eccentricity effects, but have a significant gauge component, as well. If one were to modify the PN momentum as predicted here, and use these data as the starting point for a 3.5PN evolution, the resulting binary would have an initial eccentricity of 5.5×10^{-4}, which is roughly the eccentricity we measure for the numerical binary.

In conclusion we have shown that we can use current numerical techniques to accurately model the quasi-adiabatic evolution of black-hole binaries at radii of the order of $D = 100M$ and generate the gravitational waveforms from these binaries, but the speed of the time integration techniques will need to be improved by two orders of magnitude before such simulations can be routine.

Acknowledgments

[1] F. Pretorius, Phys. Rev. Lett. **95**, 121101 (2005), gr-qc/0507014.

[2] M. Campanelli, C. O. Lousto, P. Marronetti, and Y. Zlochower, Phys. Rev. Lett. **96**, 111101 (2006), gr-qc/0511048.

[3] J. G. Baker, J. Centrella, D.-I. Choi, M. Koppitz, and J. van Meter, Phys. Rev. Lett. **96**, 111102 (2006), gr-qc/0511103.

[4] M. Shibata and K. Taniguchi, Phys. Rev. **D77**, 084015 (2008), 0711.1410.

[5] M. B. Deaton, M. D. Duez, F. Foucart, E. O'Connor, C. D. Ott, et al. (2013), 1304.3384.

[6] Z. B. Etienne, V. Paschalidis, and S. L. Shapiro, Phys. Rev. **D86**, 084026 (2012), 1209.1632.

[7] F. Pannarale, A. Tonita, and L. Rezzolla, Astrophys.J. **727**, 95 (2011), 1007.4160.

[8] K. Kiuchi, Y. Sekiguchi, M. Shibata, and K. Taniguchi, Phys. Rev. **D80**, 064037 (2009), 0904.4551.

[9] L. Baiotti, B. Giacomazzo, and L. Rezzolla, Phys. Rev. **D78**, 084033 (2008), 0804.0594.

[10] M. Anderson et al., Phys. Rev. **D77**, 024006 (2008), arXiv:0708.2720 [gr-qc].

[11] L. Baiotti and L. Rezzolla, Phys. Rev. Lett. **97**, 141101 (2006), gr-qc/0608113.

[12] C. O. Lousto and Y. Zlochower, Phys. Rev. **D77**, 024034 (2008), 0711.1165.

[13] C. O. Lousto and Y. Zlochower, Phys. Rev. Lett. **106**, 041101 (2011), 1009.0292.

[14] U. Sperhake, V. Cardoso, C. D. Ott, E. Schnetter, and H. Witek, Phys. Rev. **D84**, 084038 (2011), 1105.5391.

[15] G. Lovelace, M. Boyle, M. A. Scheel, and B. Szilagyi, Class. Quant. Grav. **29**, 045003 (2012), 1110.2229.

[16] U. Sperhake, V. Cardoso, F. Pretorius, E. Berti, and J. A. Gonzalez, Phys. Rev. Lett. **101**, 161101 (2008), 0806.1738.

[17] J. Baker, M. Campanelli, and C. O. Lousto, Phys. Rev. D **65**, 044001 (2002), gr-qc/0104063.

[18] J. Baker, B. Brügmann, M. Campanelli, and C. O. Lousto, Class. Quant. Grav. **17**, L149 (2000), gr-qc/0003027.

[19] J. Baker, B. Brügmann, M. Campanelli, C. O. Lousto, and R. Takahashi, Phys. Rev. Lett. **87**, 121103 (2001), gr-qc/0102037.

[20] J. Baker, M. Campanelli, C. O. Lousto, and R. Takahashi, Phys. Rev. D **65**, 124012 (2002), astro-ph/0202469.

[21] J. G. Baker, M. Campanelli, C. O. Lousto, and R. Takahashi, Phys. Rev. **D69**, 027505 (2004), astro-ph/0305287.

[22] M. Campanelli, Class. Quant. Grav. **22**, S387 (2005), astro-ph/0411744.

[23] M. Campanelli, B. J. Kelly, and C. O. Lousto, Phys. Rev. **D73**, 064005 (2006), gr-qc/0510122.

[24] B. Aylott et al., Class. Quant. Grav. **26**, 165008 (2009), 0901.4399.

[25] P. Ajith, M. Boyle, D. A. Brown, B. Brugmann, L. T. Buchman, et al., Class. Quant. Grav. **29**, 124001 (2012), 1201.5319.

[26] L. Lindblom, B. J. Owen, and D. A. Brown, Phys. Rev. **D78**, 124020 (2008), 0809.3844.

[27] L. Lindblom, J. G. Baker, and B. J. Owen, Phys. Rev. **D82**, 084020 (2010), 1008.1803.

[28] T. Damour, A. Nagar, and M. Trias, Phys. Rev. **D83**, 024006 (2011), 1009.5998.

[29] M. Boyle, Phys. Rev. **D84**, 064013 (2011), 1103.5088.

[30] I. MacDonald, S. Nissanke, and H. P. Pfeiffer, Class. Quant. Grav. **28**, 134002 (2011), 1102.5128.

[31] F. Ohme, M. Hannam, and S. Husa, Phys. Rev. **D84**, 064029 (2011), 1107.0996.

[32] S. C. Noble, B. C. Mundim, H. Nakano, J. H. Krolik,

M. Campanelli, Y. Zlochower, and N. Yunes, Astrophys. J. **755**, 51 (2012), 1204.1073.

[33] M. Ansorg, B. Brügmann, and W. Tichy, Phys. Rev. **D70**, 064011 (2004), gr-qc/0404056.

[34] S. Brandt and B. Brügmann, Phys. Rev. Lett. **78**, 3606 (1997), gr-qc/9703066.

[35] Y. Zlochower, J. G. Baker, M. Campanelli, and C. O. Lousto, Phys. Rev. **D72**, 024021 (2005), gr-qc/0505055.

[36] P. Marronetti, W. Tichy, B. Brügmann, J. Gonzalez, and U. Sperhake, Phys. Rev. **D77**, 064010 (2008), 0709.2160.

[37] Cactus Computational Toolkit home page: http://cactuscode.org.

[38] Einstein Toolkit home page: http://einsteintoolkit.org.

[39] F. Loffler, J. Faber, E. Bentivegna, T. Bode, P. Diener, et al., Class. Quant. Grav. **29**, 115001 (2012), 1111.3344.

[40] E. Schnetter, S. H. Hawley, and I. Hawke, Class. Quant. Grav. **21**, 1465 (2004), gr-qc/0310042.

[41] B. Brügmann et al., Phys. Rev. **D77**, 024027 (2008), gr-qc/0610128.

[42] M. Alcubierre, B. Brügmann, P. Diener, M. Koppitz, D. Pollney, E. Seidel, and R. Takahashi, Phys. Rev. **D67**, 084023 (2003), gr-qc/0206072.

[43] J. R. van Meter, J. G. Baker, M. Koppitz, and D.-I. Choi, Phys. Rev. **D73**, 124011 (2006), gr-qc/0605030.

[44] E. Schnetter, Class. Quant. Grav. **27**, 167001 (2010), 1003.0859.

[45] J. Thornburg, Class. Quant. Grav. **21**, 743 (2004), gr-qc/0306056.

[46] L. E. Kidder, Phys. Rev. **D52**, 821 (1995), gr-qc/9506022.

[47] A. Buonanno, Y. Chen, and T. Damour, Phys. Rev. **D74**, 104005 (2006), gr-qc/0508067.

[48] T. Damour, P. Jaranowski, and G. Schafer, Phys. Rev. **D77**, 064032 (2008), 0711.1048.

[49] J. Steinhoff, S. Hergt, and G. Schafer, Phys. Rev. **D77**, 081501(R) (2008), 0712.1716.

[50] H. P. Pfeiffer et al., Class. Quant. Grav. **24**, S59 (2007), gr-qc/0702106.

[51] H. Nakano, Y. Zlochower, C. O. Lousto, and M. Campanelli, Phys. Rev. **D84**, 124006 (2011), 1108.4421.

[52] Y. Zlochower, M. Ponce, and C. O. Lousto, Phys.Rev. **D86**, 104056 (2012), 1208.5494.

[53] M. Alcubierre et al., Phys. Rev. **D72**, 044004 (2005), gr-qc/0411149.

[54] G. Faye, S. Marsat, L. Blanchet, and B. R. Iyer, Class. Quant. Grav. **29**, 175004 (2012), 1204.1043.

[55] R. Fujita and B. R. Iyer, Phys. Rev. **D82**, 044051 (2010), 1005.2266.

[56] K. Arun, L. Blanchet, B. R. Iyer, and S. Sinha, Phys. Rev. **D80**, 124018 (2009), 0908.3854.

[57] C. O. Lousto, H. Nakano, Y. Zlochower, and M. Campanelli, Phys. Rev. Lett. **104**, 211101 (2010), 1001.2316.

[58] M. Babiuc, B. Szilagyi, J. Winicour, and Y. Zlochower, Phys. Rev. **D84**, 044057 (2011), 1011.4223.

[59] B. J. Kelly, W. Tichy, Y. Zlochower, M. Campanelli, and B. F. Whiting, Class. Quant. Grav. **27**, 114005 (2010), 0912.5311.

[60] D. Nunez and O. Sarbach, Phys. Rev. **D81**, 044011 (2010), 0910.5763.

[61] D. Pollney, C. Reisswig, E. Schnetter, N. Dorband, and P. Diener, Phys. Rev. **D83**, 044045 (2011), 0910.3803.

[62] B. Zink (2011), 1102.5202.

[63] S. R. Lau, G. Lovelace, and H. P. Pfeiffer, Phys. Rev. **D84**, 084023 (2011), 1105.3922.

[64] T. Damour, P. Jaranowski, and G. Schäfer, Phys. Rev. D **63**, 044021 (2001), gr-qc/0010040.

[65] G. Schäfer, *Post-Newtonian methods: Analytic results on the binary problem* (Springer, New York, 2010), chap. 6, 0910.2857.

[66] Provided by H.Nakano based on [64]

[67] Provided by H. Nakano based on [65]